Extracellular single-unit recordings from peripheral nerve axons in vitro by a novel multichannel microelectrode array

Tiantian Guo, Longtu Chen, Khanh Tran, Pejman Ghelich, Yi-Syuan Guo, Nicholas Nolta, Sharareh Emadi, Martin Han, Bin Feng*

Department of Biomedical Engineering, University of Connecticut, CT 06269, USA

*Corresponding author. Tel.: 860-486-6435; fax: 860-486-2500.

E-mail address: fengb@uconn.edu

Lab URL: https://npr.bme.uconn.edu

Abstract

The peripheral nervous system (PNS) is an attractive target for modulation of afferent input (e.g., nociceptive input signaling tissue damage) to the central nervous system. To advance mechanistic understanding of PNS neural encoding and modulation requires single-unit recordings from individual peripheral neurons or axons. This is challenged by multiple connective tissue layers surrounding peripheral nerve fibers that prevent electrical recordings by existing electrodes or electrode arrays. In this study, we developed a novel microelectrode array (MEA) via silicon-based microfabrication that consists of 5 parallel hydrophilic gold electrodes surrounded by silanized hydrophobic surfaces. This novel hydrophilic/hydrophobic surface pattern guides the peripheral nerve filaments to self-align towards the hydrophilic electrodes, which dramatically reduces the technical challenges in conducting single-unit recordings. We validated our MEA by recording simultaneous single-unit action potentials from individual axons in mouse sciatic nerves, including both myelinated A-fibers and unmyelinated C-fibers. We confirmed that our recordings were single units from individual axons by increasing nerve trunk electrical stimulus intensity, which did not alter the spike shape or amplitude. By reducing the technical challenges, our novel MEA will likely allow peripheral single-unit recordings to be adopted by a larger research community and thus expedite our mechanistic understanding of peripheral neural encoding and modulation.

Keywords: microelectrode array, single-unit, multi-channel, microfabrication, peripheral nerve, pain

1. Introduction

To interrogate the nervous system functions and mechanisms commonly requires high fidelity recordings of action potentials from individual neurons or axons, i.e., single-unit recordings. This is routinely conducted at the neural somata using a sharp liquid or metal electrode that penetrates the neural membrane to record intracellular membrane potentials (e.g., [1, 2]). Intracellular single-unit recording at the neural somata can also be conducted by a patch-clamp liquid electrode that forms a whole-cell giga-ohm seal with the neural membrane [3]. Intracellular single-unit recordings from neural axons are challenged by the much smaller axon geometry compared to that of the somata, and are conducted only in non-mammalian axons, e.g., the squid giant axons, whose axons are large enough to allow electrodes to penetrate into the axoplasm [4]. In contrast to intracellular recordings, to record action potentials extracellularly relies on the sensitive detection of ionic transmembrane currents that are usually estimated in the order of nano-Amperes in neural somata [5] and at individual Nodes of Ranvier in myelinated axons [6]. Since those tiny transmembrane currents can be easily dispersed into the surrounding electrolyte bath, extracellular single-unit recordings of action potentials require close proximity of the electrode to the neuronal tissue [7, 8].

Extracellular single-unit recordings are widely implemented in studying the neural circuitry in the central nervous system (CNS) by penetrating multi-shank electrode arrays [9], and recently by flexible neural probes or mesh-like electrodes (see [10] for a recent review). While protected by bony structures of skull and vertebrae, CNS tissues

54 inside the dura and pia mater lack additional protective layers of connective tissue and
55 allow electrodes to reach close proximity to neural somata and axons; the amplitude of
56 recorded action potential spikes in the vicinity of electrode (<50 μm) is generally large
57 enough (> 60 μV) for resolving action potentials from individual neurons via spike
58 sorting algorithms [11]. In contrast to the CNS, neural axons in mammalian peripheral
59 nervous system (PNS) are protected by multiple layers of connective tissues as
60 illustrated in Fig. 1A, i.e., epineurium, perineurium and endoneurium, which are not
61 only physical barriers that prevent the electrodes from reaching the axonal membrane
62 but also insulating layers that severely attenuate the amplitude of extracellular
63 recordings [12]. The impact of electrode location inside or outside connective tissues
64 on the quality of extracellular recordings is comprehensively summarized by a recent
65 report [13]. Consequently, most existing electrodes and electrode arrays are incapable
66 of recording single-unit action potentials from mammalian PNS axons. For example,
67 cuff electrodes non-invasively wrap around the nerve trunk outside the epineurium,
68 providing long-term biocompatibility at the expense of low-resolution recordings of
69 compound action potentials (CAPs) from a population of axons [14, 15]. Penetrating
70 electrode arrays of various geometry were developed to be placed inside the epineurium,
71 including LIFE (Longitudinal intra-fascicular electrode) [16, 17], TIME (Transverse
72 intrafascicular multichannel electrode) [18, 19], USEA (Utah slant electrode array) [20],
73 and flexible needle-structure electrodes [21-23]. Closer to nerve fascicles than the cuff
74 electrodes, penetrating electrodes provide an enhanced signal-to-noise ratio and the
75 opportunity to monitor single-unit action potentials [17, 20, 22]. Recently, a flexible

microchannel electrode array was developed for single-unit recordings from teased spinal nerve or dorsal root filaments of about 100 μm thick [24, 25]. However, most recordings appear to be from large-diameter myelinated axons (A-fibers) (e.g., in [25]), while single-unit recordings from small-diameter unmyelinated axons (C-fibers) are rarely reported by those electrodes or electrode arrays.

For sensory afferent axons, unmyelinated C-fiber afferents out-number myelinated A-fiber afferents in almost all peripheral nerves [26, 27]. Compared with A-fibers, C-fibers usually have much slower conduction velocity, lower maximum firing rate, and broader width of action potentials [28]. These features collectively make C-fiber afferents less important than A-fiber afferents in encoding physiological stimuli that require high-fidelity encoding (large range of firing frequency) and rapid transmission (fast conduction velocity). However, in pathophysiological conditions, C-fibers play critical roles and are often responsible for the persistence of a diseased state [29]. For example, C-fiber nociceptors (afferents that encode tissue-injurious stimuli and commonly, initiate the sensation of pain) can sensitize, i.e., increasing their firing rate and decreasing response threshold [30], which likely drives the persistence of many chronic pain conditions [31, 32]. Targeting C-fiber afferents for treating diseases like chronic pain requires mechanistic understanding of afferent neural encoding functions, which can be revealed by single-unit recordings from individual C-fiber axons. However, the existing penetrating electrode arrays are incapable of recording single-unit action potentials from unmyelinated C-fibers inside the endoneurium, especially those C-fibers located centrally in the Remak bundle. Currently, single-unit recordings

98 from mammalian peripheral C-fibers are typically conducted in vitro from manually
99 split nerve filaments of 10 - 50 microns using a metal wire recording electrode, which
100 is technically demanding. Recently, we expanded conventional single-wire electrode
101 recordings into a five-channel multi-wire electrode array to enhance the single-unit
102 recording efficiency [12] and successfully applied the multi-wire array to study the
103 effect of ultrasonic neuromodulation on mouse sciatic nerves [33].

104 In this study, we aim to further reduce the technical challenge and enhance the
105 efficiency of conducting single-unit recordings from peripheral nerve axons by
106 developing a novel microelectrode array via microfabrication as illustrated in Fig. 1B.
107 To eliminate the requirement of manually wrapping microns-thick nerve filaments onto
108 wire electrodes as done previously [12], we developed a surface microelectrode array
109 consisting of parallel channels with hydrophilic/hydrophobic patterns. Five recording
110 electrodes are parallel hydrophilic “islands” surrounded by hydrophobic regions, which
111 attract the split nerve filaments to attach onto hydrophilic electrodes in a hydrophobic
112 mineral oil environment; nerve filaments are hydrophilic. We implemented our
113 microfabricated electrode array in single-fiber recordings from mouse sciatic nerves in
114 vitro, and achieved simultaneous single-unit recordings from multiple sciatic nerve
115 axons of both myelinated A-fibers and unmyelinated C-fibers.

Fig. 1

116

117 **2. Materials and methods**

118 ***2.1 Fabrication of the microelectrode array (MEA)***

The MEA was fabricated on a standard 4-inch silicon wafer (UniversityWafer Inc., South Boston, MA) with procedures summarized in Fig. 2. All of the microfabrication procedures were performed in a clean room at Harvard University Center for Nanoscale Systems (Harvard CNS, Cambridge, MA).

Briefly, the silicon wafer (Fig. 2a) was first deposited with a 2 μm-thick layer of silicon dioxide (SiO_2) by low-pressure chemical vapor deposition (LPCVD) in tetraethoxysilane (Fig. 2b). We then performed photolithography to deposit a pattern of titanium (Ti) and gold (Au) onto the SiO_2 layer, consisting of five parallel electrodes, connecting interconnects, and bond pads. In photolithography, SiO_2 surface was first spun with a bilayer of photoresists (LOR3A/S1805, MicroChem Corp., Westborough, MA), patterned with a maskless aligner (MLA150, Heidelberg Instruments, Woburn, MA), and developed in MF CD-26 Developer (MicroChem Corp., Westborough, MA) (Fig. 2c). Then, we sequentially deposited Ti (10 nm thick) and Au (200 nm thick) on the patterned photoresist layers via e-beam evaporation (Denton Vacuum LLC., Moorestown, NJ) (Fig. 2d). We then conducted lift-off by soaking the wafer overnight in Remover PG (MicroChem Corp., Westborough, MA) (Fig. 2e). To electrically insulate the Ti/Au connecting wires, we deposited a layer of silicon dioxide (500 nm) using plasma-enhanced chemical vapor deposition (PECVD, SPTS Technologies, Newport, UK) (Fig. 2f). Subsequently, we conducted a second photolithography to expose the electrodes and bond pads. Similarly, the photoresist (LOR3A/S1813) pattern was created by a maskless aligner (MLA150) and developed in MF CD-26 Developer (MicroChem Corp., Westborough, MA) (Fig. 2g). The SiO_2 covering the electrodes and

141 pads was removed by reactive ion etching (RIE) in oxygen plasma (SPTS Technologies,
142 Newport, UK) (Fig. 2h). Residual photoresist was stripped with solvent Remover PG
143 (MicroChem Corp., Westborough, MA). To facilitate the attachment of split nerve
144 filaments to the hydrophilic electrode surface (Ti/Au), we modified the areas other than
145 the electrode surface to be hydrophobic by conducting a third photolithography (Fig.
146 2i). Photoresist patterns were created by a maskless aligner to cover the area of
147 electrodes and bond pads, and the entire wafer was deposited with a layer of
148 hydrophobic silane, 1H,1H,2H,2H-Perfluorodecyltrichlorosilane (#L16584, FDTS,
149 96%, Alfa Aesar, Haverhill, MA) (Fig. 2j), followed by a lift-off (Fig. 2k), as detailed
150 in Section 2.3 below. The hydrophobic surface surrounding the electrodes restricts the
151 distribution of conductive electrolytes, which not only eliminates cross recordings
152 between electrodes but also enhances the signal-to-noise ratio by increasing the
153 shunting impedance of the electrode to the bath solution [34].

Fig. 2

154

155 ***2.2 Metrology of microfabrication***

156 The quality of microfabrication was controlled by quantifying key features in each
157 step using ellipsometer, profilometer, and an optical microscope. The LSE-WS
158 Scanning Ellipsometer (ES-2), which measured the surface refractive index (n) and
159 absorption coefficient (K) (Gaertner Scientific Corp., Skokie, IL), was implemented to
160 quantify the uniformity of thickness of oxide and nitride layers over large areas
161 following deposition of photoresist or other thin film layers. In addition, visual

observation was performed under an optical microscope (100×) to check the outcome after each lift-off and etching process. Etch depth following RIE was measured by a profilometer (PL-8 DektakXT, Bruker, Billerica, MA), which was a stylus-based profilometer for step-height measurement. We moved the stylus probe down to our device surface and scanned forward for a programmed distance to determine the film thickness and etch depth.

2.3 Hydrophobic surface by vapor-phase silanization

The surfaces of the MEA, except for the electrodes and bond pads, were covered by hydrophilic SiO_2, and were modified to be hydrophobic by salinizing the SiO_2 with fluorocarbon chains. The silane reagent, 1H, 1H, 2H, 2H-Perfluorodecyltrichlorosilane ($CF_3(CF_2)_7(CH_2)_2SiCl_3$, FDTS) was chosen based upon a reported study, in which multiple silane reagents were compared; the FDTS-treated surface yielded the largest contact angle, indicative of the strongest hydrophobicity [35]. The FDTS is also biocompatible and allows cell growth on the silanized surface for up to 14 days according to a cell culture study [36]. It was also reported that vapor-phase silanization treatment yielded superior coating performance to water-phase [37]. Hence, we deposited FDTS onto the SiO_2 surface of our MEA in a custom-built vacuum chamber filled with vaporized FDTS for 20 min. Vaporization of FDTS was achieved by applying a negative pressure of 10^{-3} Torr.

2.4 Contact angle measurement

To quantify the hydrophobicity of the silanized surface, we measured the contact angle using a light microscope connected with a live camera. A drop of water of

approximately 5 microliters was placed on the surface, the outline of the droplet was captured by the camera, and the image was analyzed post-hoc to measure the contact angle (ImageJ, National Institutes of Health).

2.5 Harvest of mouse sciatic nerves

All experimental procedures were approved by the University of Connecticut Institutional Animal Care and Use Committee. C57BL/6 mice of both sexes (6-8 weeks of age, 20-30 g body weight, Taconic, Germantown, NJ) were anesthetized by isoflurane inhalation, followed by transcardiac perfusion from left ventricle to right atrium with oxygenated (95% O_2, 5% CO_2) Krebs solution (in mM: 117.9 NaCl, 4.7 KCl, 25 $NaHCO_3$, 1.3 NaH_2PO_4, 1.2 $MgSO_4$, 2.5 $CaCl_2$, 11.1 D-glucose). The carcass was transferred to a tissue dissection chamber filled with cold (~8˚C) oxygenated Krebs solution for dissection of bilateral sciatic nerves from proximal branches (L3, L4, and L5 spinal nerves) to distal branches (sural, tibial and common peroneal nerves). One dissected sciatic nerve with proximal and distal branches (~3 cm in total length) was transferred to a custom-built recording chamber consisting of two compartments, one perfused with oxygenated Krebs solution at 32˚C and the other covered with mineral oil (Fisher Scientific, Hampton, NH). The proximal branches of the sciatic nerve were pinned in the Krebs compartment while the distal branches were pulled into the adjacent mineral oil compartment for extracellular single-unit recordings.

2.6 Single-unit recordings from mouse sciatic nerve axons

To validate our microfabricated MEA, we conducted single-unit recording from distal sciatic nerve branches in vitro in the two-compartment recording chamber

described above. Action potentials were evoked by electrical stimulation of the proximal end of either L3 or L4 spinal nerves (5 - 15 volts, 0.5 Hz, monopolar anodic) in the Krebs compartment using an extracellular suction electrode (WPI, Sarasota, FL) and a stimulus isolator (A365, WPI, Sarasota, FL). Single-unit recordings were obtained from the distal branches in the adjacent mineral oil compartment. The epineurium of a distal branch was carefully removed and the nerve trunk was split into fine filaments of 10 - 50 μm thick, a process that usually removed the perineurium and severely disrupted the endoneurium [12]. When brought in proximity to the hydrophilic electrodes of the MEA in the hydrophobic mineral oil compartment, the split hydrophilic nerve filaments self-attached to the hydrophilic "islands" of the five parallel electrode lines surrounded by hydrophobic regions. To conduct simultaneous multichannel single-unit recordings, we connected the MEA via bond pads to a TDT system (Tucker-Davis Technologies Inc., Alachua, FL), which consisted of an RZ5D BioAmp processor, a PZ5 preamplifier, a high-impedance ZC32 head stage, and a ZCA-DIP16 adaptor. The single-unit recording signals were amplified at 104 dB, filtered between 300 and 3000 Hz, and digitized at 25 kHz. To reduce electrical noise, we enclosed the entire recording setup in a custom-built Faraday cage, and used DC battery packs to power the PZ5 preamplifier and A365 stimulus isolator.

2.7 Histological assessment of split nerve filaments

We qualitatively estimated the axon numbers in each split nerve filaments by imaging the cross-section using an electron microscopy protocol we reported previously [12, 33]. Briefly, the split nerve filaments were submerged in a mixed fixative solution

containing 0.12M phosphate buffer solution (PB, pH 7.2), 2.5% glutaraldehyde, 2% paraformaldehyde, and 3 mM $MgCl_2$ at 4℃ for 60 min. The tissue was then rinsed twice in PB and fixed with 1% Osmium tetroxide in 0.12 M PB for 2 h in a dark environment at room temperature. The tissue was then dehydrated by ascending series of 30, 50, 70, 95 and 100% ethyl ethanol (10 min each), each was followed by two exposures to 100% propylene oxide for 10 min. After embedding in epoxy resin at 60℃ for 48 h, the tissue was sectioned transversely on an ultramicrotome to reveal the cross-sections of the nerve filaments (Leica, Bannockburn, IL). The tissue sections were collected on grids and stained in 2% uranyl acetate and 2.5% Sato's lead citrate. The cross-sectional images of split nerve filaments were captured by a transmission electron microscope (FEI Tecnai T12, Thermo Fisher Scientific, Waltham, MA) coupled with an AMT 2 K XR40 CCD camera (4 megapixel) at an accelerating voltage of 80 kV.

2.8 Data analysis

The single-unit recordings were processed post-hoc in MATLAB v2018 (Mathworks Inc., Natick, MA). The single-unit action potential spikes were detected by setting a negative threshold of 8 (for A-fibers) or 1.5 (for C-fibers) times the root mean square of the background noise. Conduction delay of each axon was extracted by measuring the time delay between the stimulus artifact and the onset of action potential spike, which was used to calculate the afferent conduction velocity. Spike waveforms also underwent principal component analysis (PCA) and were classified based upon the first three dominant components. Data are presented as means ± SE. One-way ANOVA, two-way ANOVA or Student's t-tests were performed as appropriate using SigmaPlot

v9.0 (Systat Software, San Jose, CA). Differences were considered significant when $p < 0.05$.

3. Results and discussion

3.1 Successful microfabrication of the MEA

As shown in Fig. 3A, the microfabricated MEA consists of five parallel Ti/Au recording electrodes, each 50 μm wide and 4000 μm long, and with a 300 μm center-to-center distance between electrodes. The Ti/Au electrodes, interconnects and bond pads were protected by a layer of SiO_2 (500 nm). The recording sites of the electrodes (50×50 μm) and bond pads (1×0.5 mm) were exposed by removing the SiO_2 with RIE as indicated by light microscopy in Fig. 3B. The thickness of the deposited Ti/Au layer measured by the profilometer showed consistent thickness of ~210 nm across all five electrodes as indicated in Fig. 3C. An automatic dicing saw (Disco DAD321) was utilized to define the shape of the device. One 4 inch wafer was cut into 40 devices (7×19 mm). The MEA was connected to an 18-pin DIP socket at the bond pads via insulated Nichrome wires (0.0026'', A-M systems, Inc.), which were pasted to the bond pads by Silver Conductive Epoxy Adhesive (MG Chemicals, British Columbia, CA). We then protected the bonding junction at the bond pads with a layer of silicone (Sylgard 184, Dow Corp., Garrison, NY).

Fig. 3

3.2 Hydrophobic/hydrophilic surface patterning of the MEA

The five electrodes are hydrophilic. To modify the surrounding SiO_2 surfaces to

271 be hydrophobic, we conducted vapor-phased silanization as illustrated in Fig. 4A.
272 Tricholoro-silane groups (Si-Cl) of FDTS are converted into silanol groups (Si-OH)
273 which covalently attach to the hydroxyl groups of the SiO_2 surface via Si-O-Si bonds
274 to form a self-assembled monolayer (SAM). Unreacted terminal chlorine groups are
275 replaced with hydroxyl groups which produce a byproduct of HCl. These hydroxyl
276 groups then condense and cross-link with silanols on other precursor molecules to
277 generate a siloxane network. After silanization, the heavy fluorinated tail of FDTS
278 increases the surface hydrophobicity as quantified by increase in contact angle. As
279 shown in Fig. 4B, the contact angle of the MEA surface interfaced with a water droplet
280 was significantly increased following silanization treatment ($52° \pm 3.1°$ vs $92.6° \pm 2.9°$,
281 $p < 0.001$). Further, to assess the stability of silanized surface, we submerged the
282 silanized surfaces in mineral oil overnight, removed the mineral oil with ethanol and
283 measured the contact angle again; there was no significant change from before the
284 mineral oil treatment ($92° \pm 3.1°$ vs. $92.6° \pm 2.9°$, $p > 0.9$). This strongly indicates that
285 silanization with vaporized FDTS results in stable hydrophobic surfaces of the MEA
286 suitable for prolonged in vitro single-unit recordings in the mineral oil compartment of
287 our recording chamber.

Fig. 4

288

289 ***3.3 Electrical impedance of the MEA***

290 The electrical impedance of the MEA affects the quality of extracellular recordings.
291 Generally, reduced contact area of the electrode/electrolyte interface will restrict the

292 ‘listening’ area to facilitate recordings from individual neurons or axons, i.e., single-
293 unit recordings [8]. However, this is at the expense of increased electrode impedance
294 that leads to increased thermal noise in the recordings attenuating the signal-to-noise
295 ratio [38]. Based on our extensive experience with metal wire recordings, relatively
296 large electrode size permits single-unit recordings from peripheral nerve axons, likely
297 due to the significantly lower density of axons/neurons in the PNS as compared to in
298 the CNS [39, 40]. Hence, we designed our electrode/electrolyte interface to be 50 by
299 50 μm, a surface area comparable to that of conventional wire electrodes. We
300 determined the impedance of our MEA in phosphate-buffered saline using a potentiostat
301 instrument (Metrohm Autolab, Utrecht, Netherlands). Each electrode of the MEA was
302 tested individually along with a large platinum counter electrode (PINE Research, NC,
303 USA) and a silver/silver chloride reference electrode (Cole-Parmer, IL, USA). The
304 electrode impedances were measured from 0.1 Hz to 100 kHz to generate an impedance
305 spectroscopy with a representative Bode plot shown in Fig. 5. The average impedance
306 of our MEA was 23.6 kΩ ± 8.8 kΩ (N = 11) at 1 kHz, which falls in the anticipated
307 range for metal electrodes with an exposed tip dimension of 2500 μm^2 in area.

Fig. 5

308

309 ***3.4 Simultaneous recording from multiple sciatic nerve axons in vitro***

310 Following the procedures reported in Sections 2.5 and 2.6, we conducted single-
311 unit recordings from mouse sciatic nerve axons using our microfabricated MEA as
312 shown in Fig. 6A. In the Krebs compartment, action potentials were evoked by a suction

electrode at 0.5 Hz (5 - 15 volts, monopolar anodic 0.2 ms duration). In the mineral oil compartment, five split filaments were attached to the 5 hydrophilic electrodes in the MEA. The reference electrode was placed perpendicular to the 5 recording electrodes to permit bipolar recordings of action potentials. The ground electrode was placed in the bath solution in the Krebs compartment.

Fig. 6

For multichannel recordings, electrical insulation between electrodes is crucial to avoid action potentials from the same axon being recorded in multiple channels [12]. As shown in Fig. 6A, the large hydrophobic surface that surrounds individual electrodes prevent conductive electrolyte solution from accumulating between electrodes, thus reducing chances for cross-electrode recordings. To achieve distinct recordings from individual axons, the sciatic nerve was split into fine filaments of 10 – 50 μm thick (Fig. 6B), which as indicated by the electron microscopy image in Fig. 6B loosened up the individual axons to facilitate closer contact to the electrodes. The small number of axons in each filament (<100) also enhances the chances of recording temporarily distinct action potential spikes, i.e., single-units. As shown in Fig. 6C, single-unit recordings using the MEA showed clearly different spike patterns, in both amplitude and conduction delay, between adjacent MEA electrodes. The MEA was capable of recording from both fast-conducting A-fibers (conduction velocity, CV, > 1m/s) as well as slow-conducting C-fibers (CV < 1m/s).

3.5 Validation of single-unit recordings with ascending stimulus intensities

To confirm that recorded spikes are from individual axons, we conducted additional experiments by gradually increasing the electrical stimulus intensity by 0.5 or 1 volts. There are two criteria to isolate single-unit action potentials: consistent shape and unchanged amplitude [41]. For a typical 5-channel single-unit recording shown in Fig. 6C, action potential spikes were marked by unfilled arrows (from potentially 10 different axons), extracted from recordings conducted at different electrical stimulus intensities, and overlaid with one another in Fig. 7A. We then conducted a principal component analysis on all spikes recorded from multiple stimulus intensities and used the first three dominant components to separate the spikes into ten clusters (N = 54, 81, 29, 301, 134, 356, 465, 203, 114, 185) as shown in Fig. 7B, which confirmed the unique identity of spike shapes from different peripheral axons. In addition, the single-unit spike amplitudes recorded at different stimulus intensities were plotted in 7C, which showed no significant difference in amplitude. The fact that individual spikes in our recordings do not change in shape or amplitude confirms that they are single-unit recordings from 10 different, individual axons.

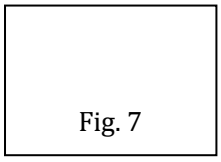

Fig. 7

As shown in Fig. 7D, the peak-to-peak amplitude of single-unit action potentials is proportional to their conduction velocities. This is not unexpected given that fast-conducting A-fibers are stronger electrical current sources than slowly-conducting C-fibers, because of the significantly larger axon diameter and the presence of Nodes of

Ranvier with concentrated ion channels. As shown in Fig. 7E, the stimulus thresholds that activate individual axons appear to be inversely proportional to their conduction velocities, consistent with other findings that A-fiber axons have lower stimulus activation thresholds than C-fiber axons [42, 43].

3.6 Distribution of conduction velocity from different types of axons

The conduction velocities (CV) of recorded action potentials reflect their myelination and physical diameters: axons with CV greater than 1 m/s in mice are generally myelinated A-fibers with large diameters (5 – 20 microns) whereas axons with CV less than 1 m/s are unmyelinated C-fibers with small diameters (~1 microns) [12]. To validate that our MEA is capable to record action potentials from different types of axons with different conduction velocities, we conducted recordings on 49 split nerve filaments from 18 sciatic nerves, from which 147 single-unit spikes were recorded. A typical recording shown in Fig. 8A allows the calculation of CV from conduction delays, and the CV of the 147 axons were plotted in a histogram in Fig. 8B, including 43 A-fibers (CV > 1 m/s) and 104 C-fibers (CV < 1m/s).

Fig. 8

4. Conclusions

In summary, we have successfully developed a multichannel microelectrode array via silicon-based microfabrication that allows convenient single-unit, simultaneous

recordings from mammalian peripheral nerve axons in vitro. The MEA consists of planar titanium/gold electrodes sandwiched between insulating silicon dioxide layers. The exposed electrode/electrolyte surface is 50 by 50 microns, yielding a relatively low electrode impedance around 24kΩ at 1 kHz to lessen recording noise, and may further be improved with use of iridium oxide or PEDOT. The innovative MEA surface design of parallel hydrophilic electrode channels surrounded by hydrophobic areas facilitates the alignment of split nerve filaments with electrode channels, reducing the technical challenge of traditional single-unit recordings from peripheral mammalian axons. The hydrophobic surface pattern was generated by silanization of a silicon dioxide surface by vaporized FDTS. The novel MEA achieved simultaneous five-channel recordings from 5 different peripheral nerve filaments, a high throughput approach compared with conventional recordings with wire electrodes. In addition, both myelinated A-fibers and unmyelinated C-fibers were recorded with the MEA. Increased electrical stimulus intensity did not alter the shape or amplitude of recorded action potential spikes, which strongly indicated that those spikes were single units from different, individual axons. We anticipate that with further development of this MEA, single-unit recordings from peripheral nerve axons will be implemented by a broader research community that will work collaboratively to advance our mechanistic understanding of peripheral neural encoding, transmission and modulation for treating diseases.

Acknowledgments

We sincerely thank Dr. G. F. Gebhart for editing the manuscript and providing

constructive feedbacks. This work was supported by NSF CAREER 1844762 and NIH R01 DK120824 grants awarded to Dr. Bin Feng, as well as NIH R01 R01DC014044 grant awarded to Dr. Martin Han.

Illustration of the figures

Fig. 1 (A) Schematic of a peripheral nerve and the three layers of connective tissues around and within the nerve: epineurium, perineurium and endoneurium. (B) Schematic of the novel microelectrode array (MEA) for in vitro simultaneous, single-unit recordings from multiple split nerve filaments.

Fig. 2 Schematic of the silicon-based microfabrication processes for the MEA. SiO_2: silicon dioxide; Ti: titanium; Au: gold; FDTS: 1H, 1H, 2H, 2H-Perfluorodecyltrichlorosilane. Refer to the texts for more details.

Fig. 3 Validation of MEA fabrication by light microscopy and profilometry. (A) The pattern of deposited gold electrodes and bonding pads sandwiched and insulated by two layers of silicon dioxide. (B) Opening of the electrode/electrolyte interface (50×50 μm) by removing the silicon dioxide layer on the gold electrode by reactive ion etching. (C) Thickness of the metal deposition measured by stylus surface profilometry. The inset shows the stylus tip.

Fig. 4 Surface modification by silanization to convert hydrophilic silicon dioxide surface to be hydrophobic. (A) Silanization reactions for generating a hydrophobic FDTS monolayer on the silicon dioxide surface via covalent bonding. (B) Surface hydrophobicity quantified by contact angle measurement of the electrode array interfaced with a water droplet before and after silanization.

Fig. 5 Electrical impedance spectroscopy of the MEAs. The top and bottom panels are impedance magnitude and phase angle, respectively. The inset shows the magnitude of impedance around 1 kHz.

Fig. 6 Validation of the MEA by in vitro single-unit recordings from mouse sciatic nerve axons. (A) A photograph of the single-unit recording setup in the two-compartment recording chamber. The branches of L3-L5 spinal nerves were placed in the tissue compartment and the distal branches of sciatic nerve were pulled into the adjacent mineral oil compartment. Action potentials were evoked by electrically stimulating spinal nerves with a suction electrode. The magnified view shows the interface between five split nerve filaments and the five channels of electrodes in the MEA. (B) The cross-section of a split nerve filament revealed by electron microscopy. (C) Simultaneous single-unit recordings from five electrode channels. The vertical dotted line indicates an approximate conduction velocity of 1 m/s (30mm axon length), i.e., the criterion for distinguishing myelinated A-fibers from unmyelinated C-fibers. Single-unit spikes are marked by unfilled arrows. The stimulus artifact is marked by a filled arrow.

Fig. 7 Validation of single-unit recordings by increasing the electrical stimulus intensity and post-hoc spike analysis. (A) The waveforms of the 10 action potentials spikes indicated in Fig. 6C by unfilled arrows were extracted and overlaid after application of six different electrical stimulus intensities. Spike waveforms are unchanged by varying stimulus intensity. (B) Principal component analysis of spike waveforms to cluster the same spikes in (A) into 10 groups based upon the first three principal components in the Cartesian coordinate. (C) Amplitudes of the 10 labeled spikes in Fig. 6C evoked by varying stimulus intensities from 5 to 15 volts. (D) Spike amplitude is proportional to conduction velocity ($R^2 = 0.49$). (E)

445 Electrical stimulus threshold appears to be inversely proportional to conduction
446 velocity ($R^2 = 0.37$). PC: principal component.
447 Fig. 8 Ability to record from both A-type and C-type axons by the MEA. (A) Typical
448 recordings from both myelinated A-fibers (unfilled arrows) and unmyelinated C-
449 fibers (filled arrows). (B) The histogram of conduction velocities (m/s) from 43
450 A-fibers (orange) and 104 C-fibers (magenta).
451

References

[1] S. Malin, D. Molliver, J.A. Christianson, E.S. Schwartz, P. Cornuet, K.M. Albers, et al., TRPV1 and TRPA1 function and modulation are target tissue dependent, JNeurosci, 31(2011) 10516-28.

[2] M.P. Jankowski, K.K. Rau, K.M. Ekmann, C.E. Anderson, H.R. Koerber, Comprehensive Phenotyping of Group III and IV Muscle Afferents in Mouse, Journal of neurophysiology, (2013).

[3] B. Sakmann, E. Neher, Patch clamp techniques for studying ionic channels in excitable membranes, Annu Rev Physiol, 46(1984) 455-72.

[4] J.R. Clay, Potassium current in the squid giant axon, International review of neurobiology, 27(1985) 363-84.

[5] B. Feng, Y. Zhu, J.H. La, Z.P. Wills, G.F. Gebhart, Experimental and computational evidence for an essential role of NaV1.6 in spike initiation at stretch-sensitive colorectal afferent endings, Journal of neurophysiology, 113(2015) 2618-34.

[6] H. Kanda, J. Ling, S. Tonomura, K. Noguchi, S. Matalon, J.G. Gu, TREK-1 and TRAAK Are Principal K+ Channels at the Nodes of Ranvier for Rapid Action Potential Conduction on Mammalian Myelinated Afferent Nerves, Neuron, 104(2019) 960-71.e7.

[7] B.C. Wheeler, Y. Nam, In Vitro Microelectrode Array Technology and Neural Recordings, 39(2011) 45-61.

[8] M.M. Heinricher, Principles of extracellular single-unit recording, Microelectrode Recording in Movement Disorder Surgery, 8(2004).

[9] M. Han, P.S. Manoonkitiwongsa, C.X. Wang, D.B. McCreery, In vivo validation of custom-designed silicon-based microelectrode arrays for long-term neural recording and stimulation, IEEE transactions on biomedical engineering, 59(2011) 346-54.

[10] G.H. Kim, K. Kim, E. Lee, T. An, W. Choi, G. Lim, et al., Recent Progress on Microelectrodes in Neural Interfaces, Materials (Basel), 11(2018) 1995.

[11] G. Buzsáki, Large-scale recording of neuronal ensembles, Nature neuroscience,

7(2004) 446-51.

[12] L. Chen, S.J. Ilham, T. Guo, S. Emadi, B. Feng, In vitro multichannel single-unit recordings of action potentials from mouse sciatic nerve, Biomed Phys Eng Express, 3(2017) 045020.

[13] B.S. Spearman, V.H. Desai, S. Mobini, M.D. McDermott, J.B. Graham, K.J. Otto, et al., Tissue-Engineered Peripheral Nerve Interfaces, Advanced Functional Materials, 28(2018) 1701713.

[14] Y. Zhang, N. Zheng, Y. Cao, F. Wang, P. Wang, Y. Ma, et al., Climbing-inspired twining electrodes using shape memory for peripheral nerve stimulation and recording, Science advances, 5(2019) eaaw1066.

[15] X. Kang, J. Liu, H. Tian, B. Yang, Y. Nuli, C. Yang, Self-Closed Parylene Cuff Electrode for Peripheral Nerve Recording, Journal of Microelectromechanical Systems, 24(2015) 319-32.

[16] N. Lago, K. Yoshida, K.P. Koch, X. Navarro, Assessment of Biocompatibility of Chronically Implanted Polyimide and Platinum Intrafascicular Electrodes, IEEE Transactions on Biomedical Engineering, 54(2007) 281-90.

[17] K. Yoshida, D. Farina, M. Akay, W. Jensen, Multichannel Intraneural and Intramuscular Techniques for Multiunit Recording and Use in Active Prostheses, Proceedings of the IEEE, 98(2010) 432-49.

[18] J. Badia, S. Raspopovic, J. Carpaneto, S. Micera, X. Navarro, Spatial and Functional Selectivity of Peripheral Nerve Signal Recording With the Transversal Intrafascicular Multichannel Electrode (TIME), IEEE transactions on neural systems and rehabilitation engineering : a publication of the IEEE Engineering in Medicine and Biology Society, 24(2016) 20-7.

[19] A. Cutrone, J.D. Valle, D. Santos, J. Badia, C. Filippeschi, S. Micera, et al., A three-dimensional self-opening intraneural peripheral interface (SELINE), Journal of neural engineering, 12(2015) 016016.

[20] H.A.C. Wark, R. Sharma, K.S. Mathews, E. Fernandez, J. Yoo, B. Christensen, et al., A new high-density (25 electrodes/mm2) penetrating microelectrode array for recording and stimulating sub-millimeter neuroanatomical structures, Journal of neural engineering, 10(2013) 045003.

[21] J. Wang, X.Y. Thow, H. Wang, S. Lee, K. Voges, N.V. Thakor, et al., A Highly

514 Selective 3D Spiked Ultraflexible Neural (SUN) Interface for Decoding Peripheral
515 Nerve Sensory Information, Advanced Healthcare Materials, 7(2018) 1700987.

516 [22] D. Byun, S.J. Cho, B.H. Lee, J. Min, J.H. Lee, S. Kim, Recording nerve signals
517 in canine sciatic nerves with a flexible penetrating microelectrode array, Journal of
518 neural engineering, 14(2017) 046023.

519 [23] D. Yan, A. Jiman, D. Ratze, S. Huang, S. Parizi, E. Welle, et al., Microneedle
520 Penetrating Array with Axon-Sized Dimensions for Cuff-less Peripheral Nerve
521 Interfacing, 2019 9th International IEEE/EMBS Conference on Neural Engineering
522 (NER)2019, pp. 827-30.

523 [24] D.J. Chew, L. Zhu, E. Delivopoulos, I.R. Minev, K.M. Musick, C.A. Mosse, et
524 al., A microchannel neuroprosthesis for bladder control after spinal cord injury in rat,
525 Science translational medicine, 5(2013) 210ra155.

526 [25] S. Gribi, S. du Bois de Dunilac, D. Ghezzi, S.P. Lacour, A microfabricated nerve-
527 on-a-chip platform for rapid assessment of neural conduction in explanted peripheral
528 nerve fibers, Nature Communications, 9(2018) 4403.

529 [26] B.B. Murinson, J.W. Griffin, C-Fiber Structure Varies with Location in
530 Peripheral Nerve, Journal of Neuropathology & Experimental Neurology, 63(2004)
531 246-54.

532 [27] M.A. Reina, R. Arriazu, C.B. Collier, X. Sala-Blanch, L. Izquierdo, J. de Andres,
533 Electron microscopy of human peripheral nerves of clinical relevance to the practice
534 of nerve blocks. A structural and ultrastructural review based on original experimental
535 and laboratory data, Revista espanola de anestesiologia y reanimacion, 60(2013) 552-
536 62.

537 [28] B.Y. Li, B. Feng, H.Y. Tsu, J.H. Schild, Unmyelinated visceral afferents exhibit
538 frequency dependent action potential broadening while myelinated visceral afferents
539 do not, Neuroscience letters, 421(2007) 62-6.

540 [29] J. Tavee, L. Zhou, Small fiber neuropathy: a burning problem, Cleve Clin J Med,
541 76(2009) 297-305.

542 [30] M.S. Gold, G.F. Gebhart, Nociceptor sensitization in pain pathogenesis, Nat
543 Med, 16(2010) 1248-57.

544 [31] B. Feng, J.H. La, E.S. Schwartz, G.F. Gebhart, Irritable bowel syndrome:
545 methods, mechanisms, and pathophysiology. Neural and neuro-immune mechanisms

of visceral hypersensitivity in irritable bowel syndrome, American journal of physiology Gastrointestinal and liver physiology, 302(2012) G1085-98.

[32] P.R. Brumovsky, B. Feng, L. Xu, C.J. McCarthy, G.F. Gebhart, Cystitis increases colorectal afferent sensitivity in the mouse, American journal of physiology Gastrointestinal and liver physiology, 297(2009) G1250-8.

[33] S.J. Ilham, L. Chen, T. Guo, S. Emadi, K. Hoshino, B. Feng, In vitro single-unit recordings reveal increased peripheral nerve conduction velocity by focused pulsed ultrasound, Biomed Phys Eng Express, 4(2018) 045004.

[34] L. Wang, M. Riss, J.O. Buitrago, E. Claverol-Tinture, Biophysics of microchannel-enabled neuron-electrode interfaces, Journal of neural engineering, 9(2012) 026010.

[35] D. Janssen, R. De Palma, S. Verlaak, P. Heremans, W. Dehaen, Static solvent contact angle measurements, surface free energy and wettability determination of various self-assembled monolayers on silicon dioxide, Thin Solid Films, 515(2006) 1433-8.

[36] G. Jing, Y. Wang, T. Zhou, S.F. Perry, M.T. Grimes, S. Tatic-Lucic, Cell patterning using molecular vapor deposition of self-assembled monolayers and lift-off technique, Acta biomaterialia, 7(2011) 1094-103.

[37] G.Y. Jung, Z. Li, W. Wu, Y. Chen, D.L. Olynick, S.Y. Wang, et al., Vapor-phase self-assembled monolayer for improved mold release in nanoimprint lithography, Langmuir, 21(2005) 1158-61.

[38] P.R.F. Rocha, P. Schlett, U. Kintzel, V. Mailänder, L.K.J. Vandamme, G. Zeck, et al., Electrochemical noise and impedance of Au electrode/electrolyte interfaces enabling extracellular detection of glioma cell populations, Scientific reports, 6(2016) 34843.

[39] B. Feng, S.C. Joyce, G.F. Gebhart, Optogenetic activation of mechanically insensitive afferents in mouse colorectum reveals chemosensitivity, American journal of physiology Gastrointestinal and liver physiology, 310(2016) G790-8.

[40] B. Feng, G.F. Gebhart, In vitro functional characterization of mouse colorectal afferent endings, Journal of visualized experiments : JoVE, (2015) 52310.

[41] M. Schafers, D. Cain, Single-fiber recording: in vivo and in vitro preparations, Methods in molecular medicine, 99(2004) 155-66.

[42] S. Qiao, O. Odoemene, K. Yoshida, Determination of electrode to nerve fiber distance and nerve conduction velocity through spectral analysis of the extracellular action potentials recorded from earthworm giant fibers, Medical & biological engineering & computing, 50(2012) 867-75.

[43] S. Qiao, K. Yoshida, Influence of unit distance and conduction velocity on the spectra of extracellular action potentials recorded with intrafascicular electrodes, Medical engineering & physics, 35(2013) 116-24.

Figure 1
Click here to download high resolution image

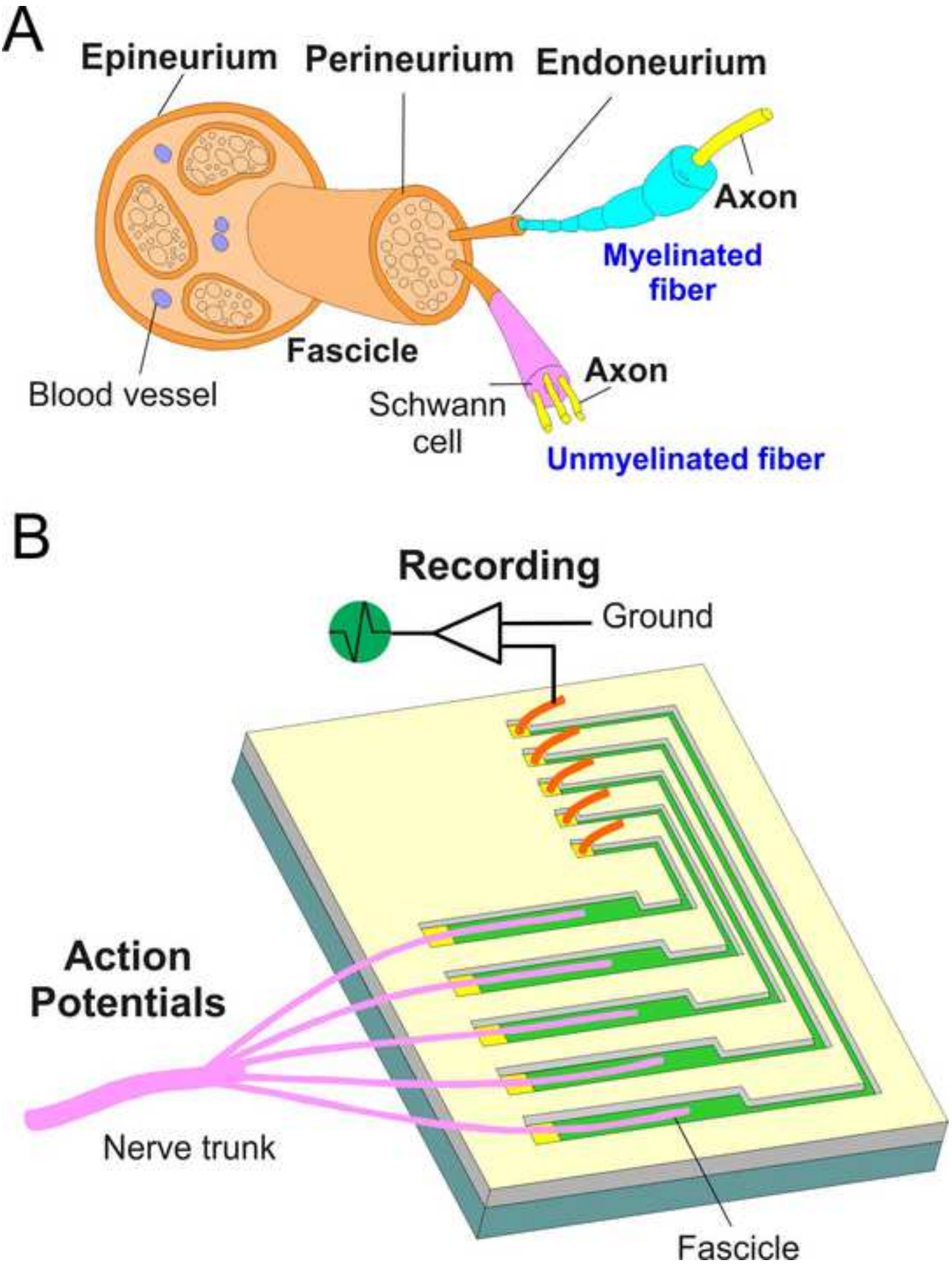

Figure 2

Click here to download high resolution image

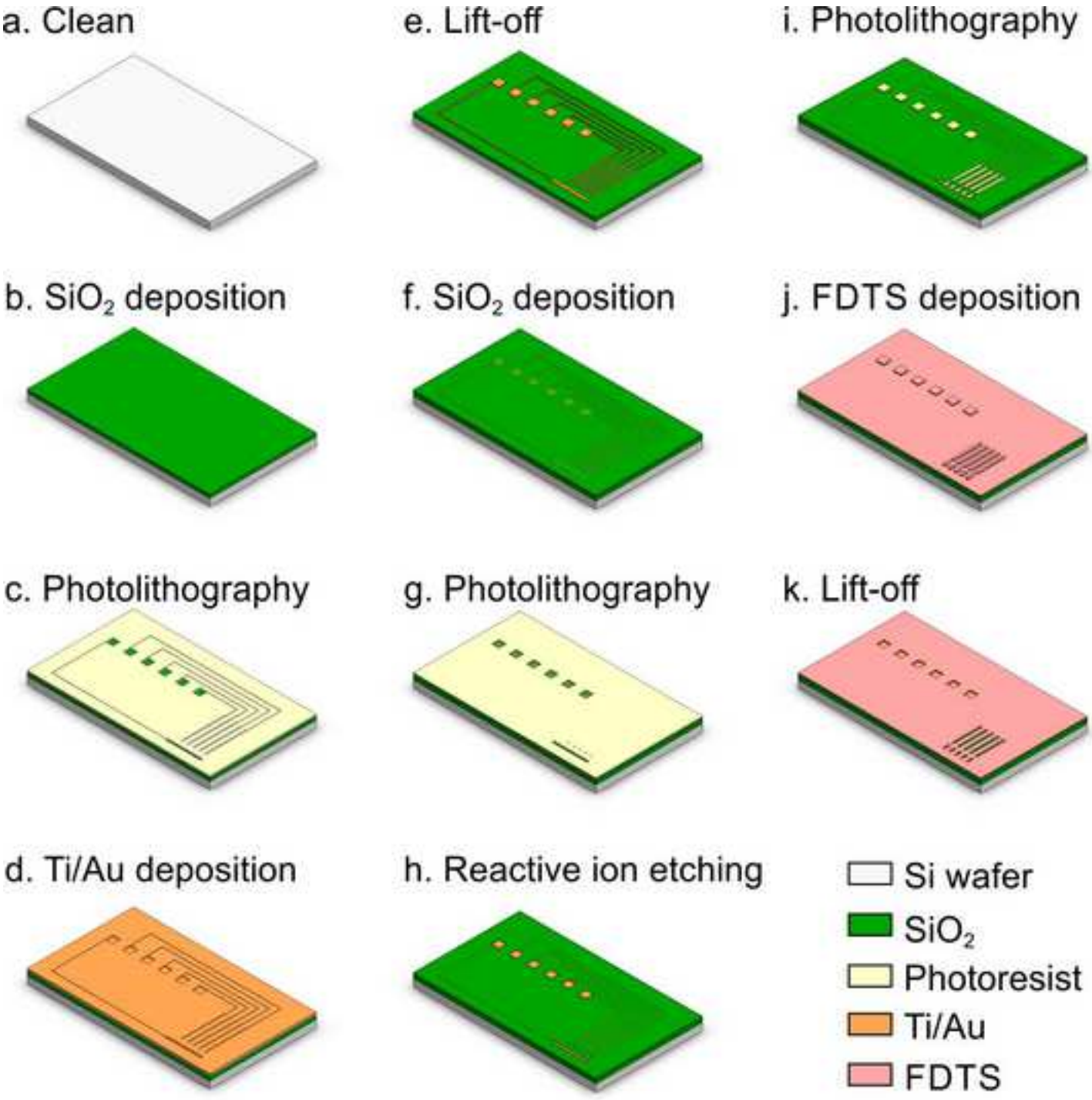

Figure 3
Click here to download high resolution image

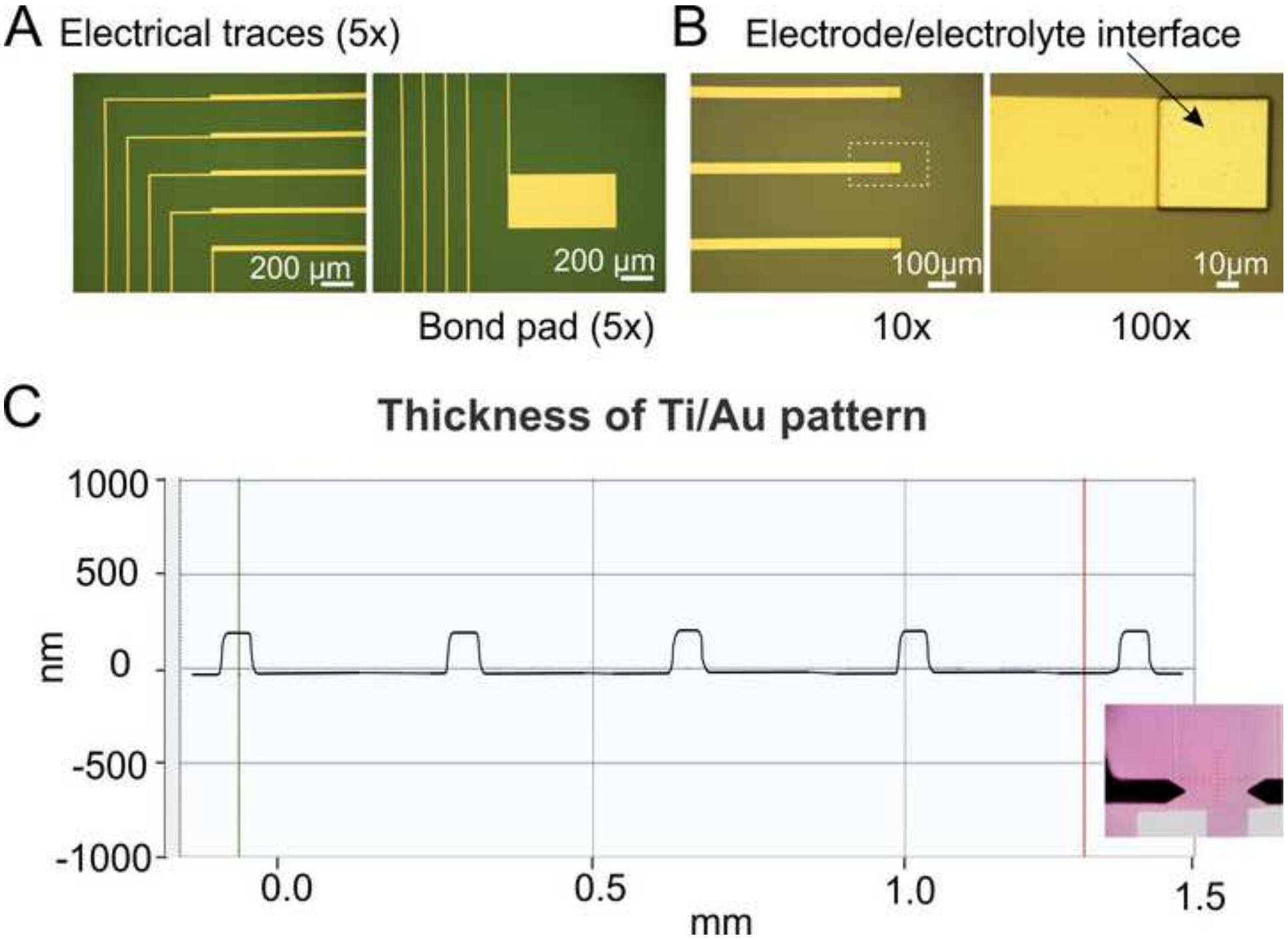

Figure 4
Click here to download high resolution image

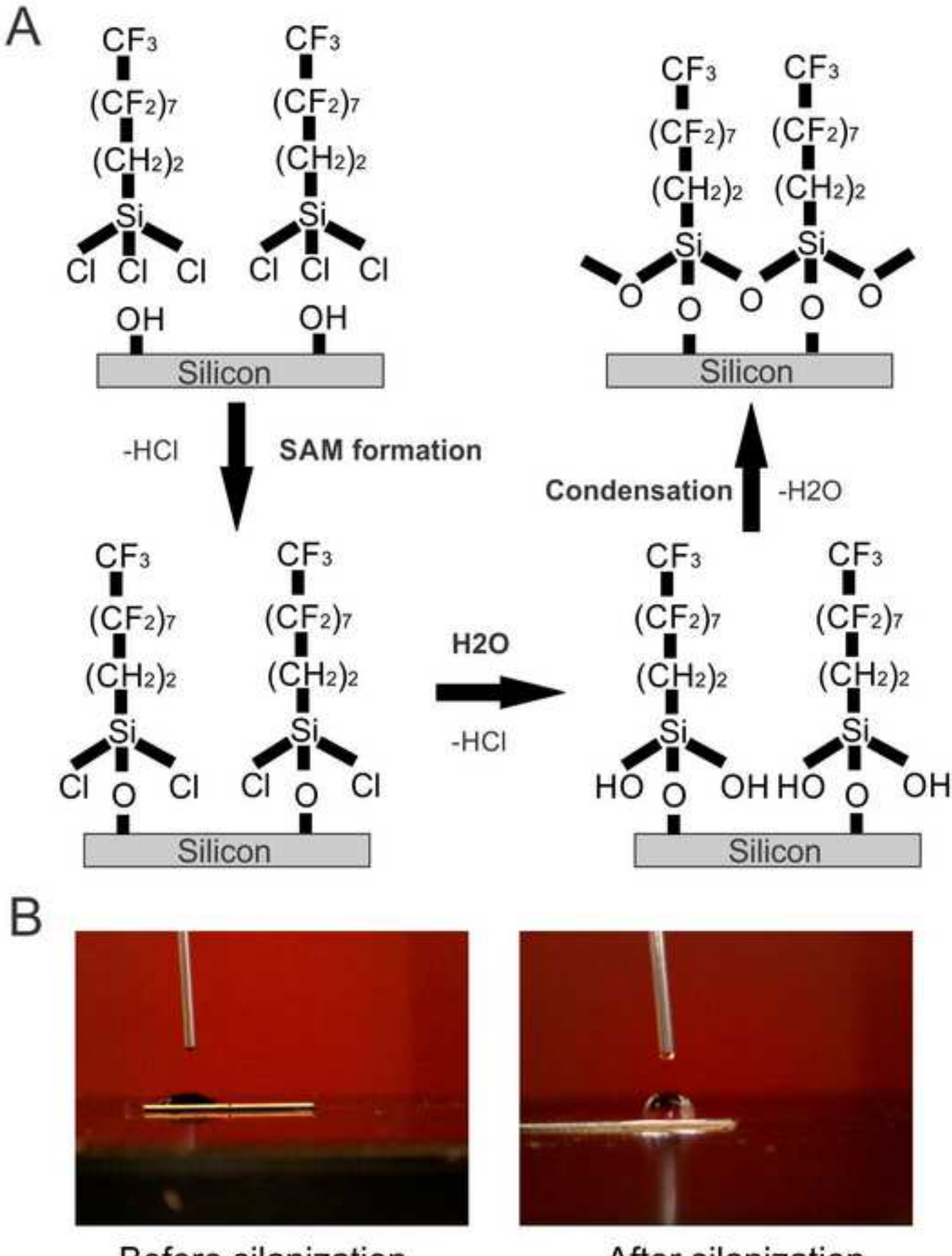

Figure 5
Click here to download high resolution image

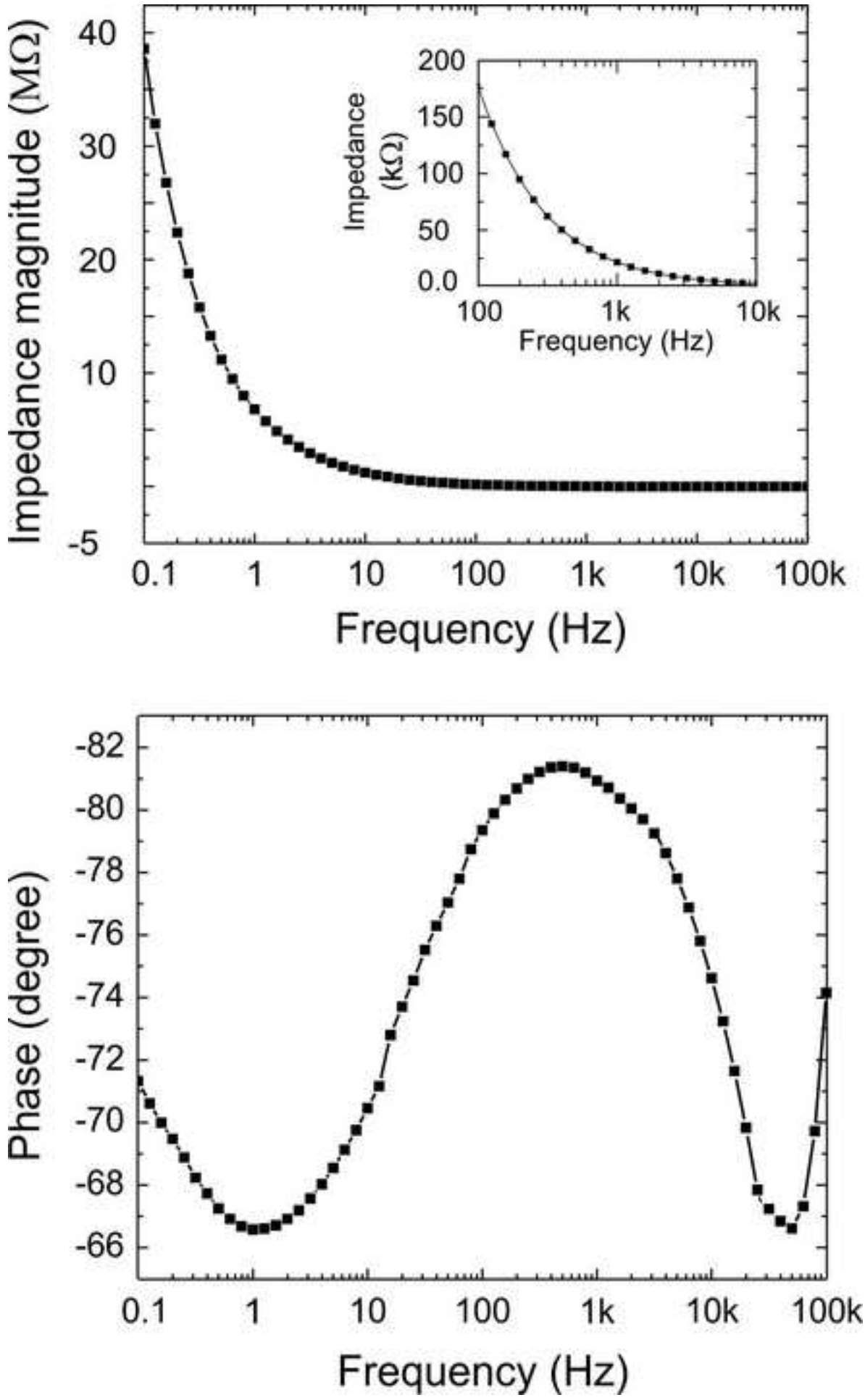

Figure 6

Click here to download high resolution image

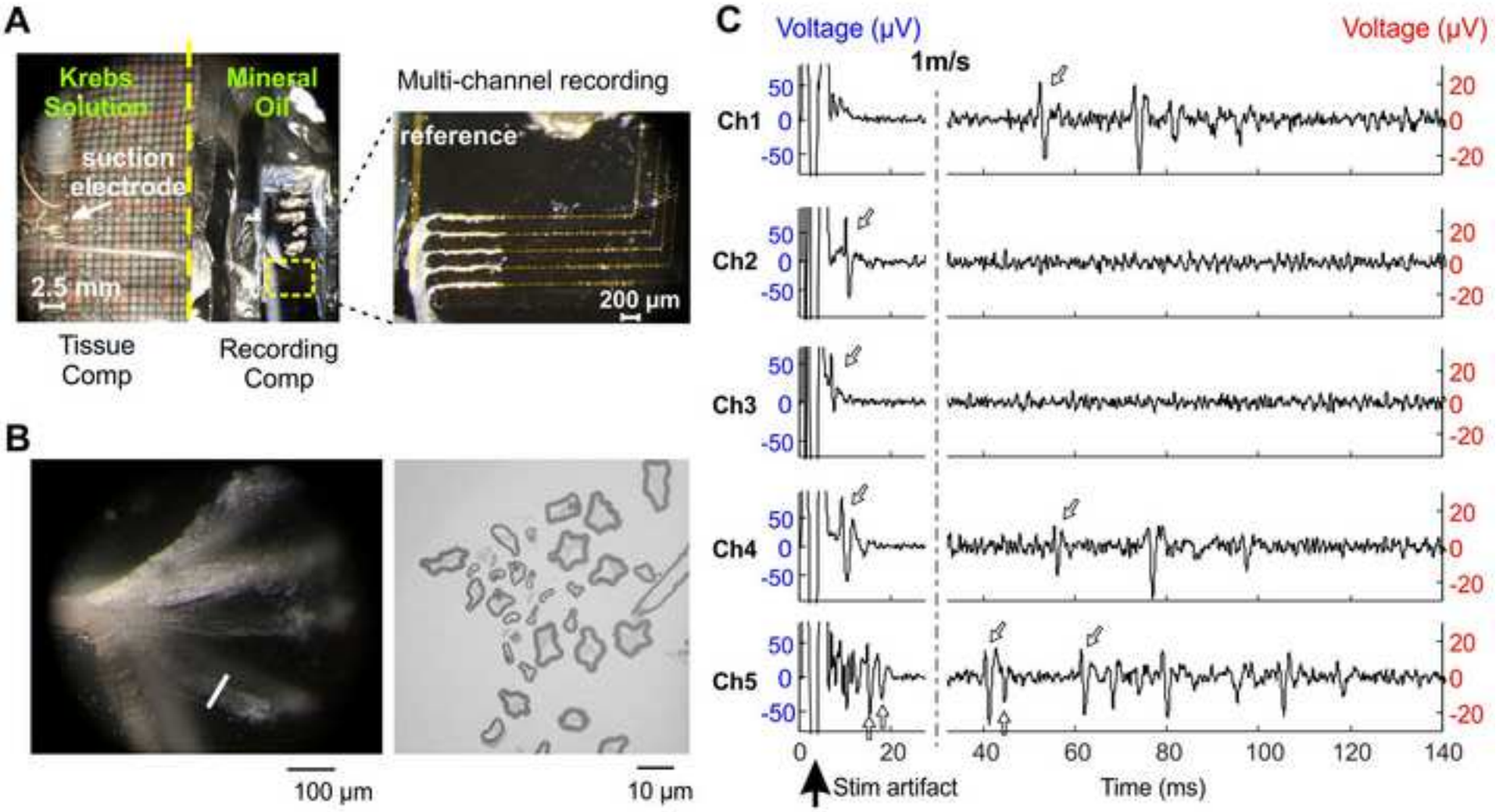

Figure 7

Click here to download high resolution image

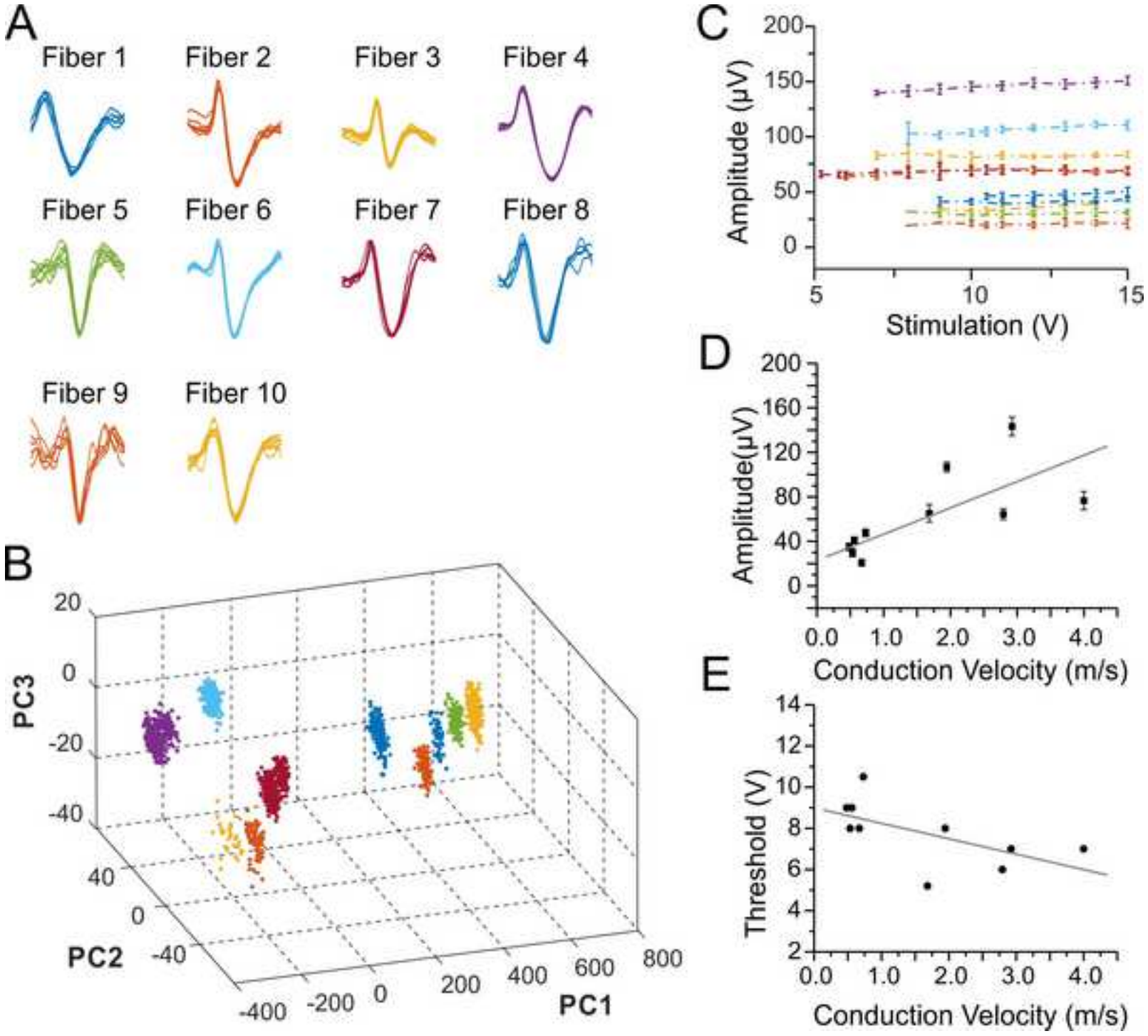

Figure 8
Click here to download high resolution image